

Manipulation of magnetic skyrmion in a two-dimensional van der Waals heterostructure via both electric and magnetic fields

Wei Sun¹, Wenxuan Wang¹, Jiadong Zang², Hang Li^{1*}, Guangbiao Zhang¹, Jianli Wang¹, Zhenxiang Cheng^{3*}

¹International Joint Research Laboratory of New Energy Materials and Devices of Henan Province, School of Physics and Electronics, Henan University, Kaifeng 475004, PR China

²Department of Physics and Astronomy, University of New Hampshire, Durham, New Hampshire 03824, USA

³Institute for Superconducting & Electronic Materials, Australian Institute of Innovative Materials, University of Wollongong, Innovation Campus, Squires Way, North Wollongong, NSW 2500, Australia

*Corresponding author. Email: hang.li@vip.henu.edu.cn (H.L.); cheng@uow.edu.au (Z.X.C.)

Keywords: magnetic skyrmions, van der Waals heterostructures, two-dimensional, magnetism, multiferroic.

Abstract

As a promising candidate for the much-desired low power consumption spintronic devices, two-dimensional magnetic van der Waals material also provides a versatile platform for the design and control of topological spin textures. In this work on $WTe_2/CrCl_3$ bilayer van der Waals heterostructure, we demonstrate a complete Néel-type skyrmion – bimeron – ferromagnet phase transition, accompanied by the evolution of the topological number. This cyclic transition, mediated by a perpendicular magnetic field, is largely driven by the competition between the out-of-plane magnetocrystalline anisotropy and magnetic dipole-dipole interaction. In the presence of a driving current, the Néel-type skyrmion gains a higher velocity yet larger skyrmion Hall angle, in a comparison to the bimeron. By incorporating a ferroelectric $CuInP_2S_6$ monolayer as substrate, we may regulate writing and erasing of skyrmions using a ferroelectric polarization. Our work sheds light

This is the author manuscript accepted for publication and has undergone full peer review but has not been through the copyediting, typesetting, pagination and proofreading process, which may lead to differences between this version and the [Version of Record](#). Please cite this article as [doi: 10.1002/adfm.202104452](https://doi.org/10.1002/adfm.202104452).

on a novel approach to the design and control of magnetic skyrmions on two-dimensional van der Waals materials.

1. Introduction

Magnetic skyrmion is a whirling spin texture.^[1,2] Its transport and topologically protected magnetic properties^[3-12] make it an ideal information carrier in the next-generation information storage and processing device, such as the racetrack memory.^[13] Magnetic skyrmion debuts in several spin configurations, namely, Néel, Bloch and more recently discovered bimeron. They have been found in various materials, including two-dimensional (2D) van der Waals (vdW) magnet which is at the forefront of materials research. Two-dimensional vdW magnet is a monolayer that integrates surface and miniaturised magnetism,^[14-18] which has pushed the study in magnetic skyrmions to the atomically thin limit.^[19-25] Outstanding vdW magnets include CrI₃,^[14] Cr₂Ge₂Te₆,^[15] and Fe₃GeTe₂.^[16]

Dzyaloshinskii-Moriya interaction (DMI) is central to the creation, stabilization, and manipulation of skyrmions. DMI emerges, and can even be tuned, in 2D magnets with broken inversion symmetry.^[26-29] This includes Janus monolayer structure^[20,21,30,31] and magnetic monolayer under perpendicular electric fields.^[32] The ease of interfacial engineering that is intrinsic to vdW heterostructures (HSs) makes it flexible to induce DMI via Rashba spin-orbit coupling at the interface between magnetic monolayer and heavy-metal (or ferroelectric) layer, such as WTe₂/Fe₃GeTe₂,^[19] LaCl/In₂Se₃,^[33] and Cr₂Ge₂Te₆/In₂Se₃ HSs.^[34] Furthermore, electron reconstruction (HL: Citation on electron reconstruction?) that occurs at the heterointerface provides an additional mechanism to mediate the magnetic interactions at atomic level. By manipulating the competition among DMI and various kinds of magnetic interactions in 2D materials, such as exchange interaction,

magnetocrystalline anisotropy (MCA), magnetic dipole-dipole interaction (DDI), a variety of magnetic textures can be created.

Magnetic anisotropy plays, alongside DMI, a vital role in stabilizing skyrmions. In a 2D magnet with a perpendicular anisotropy, skyrmion favours the Néel-type for a clear energy incentive to align the magnetisation with the anisotropy axis.^[35-37] The easy-plane anisotropy, on the other hand, tends to confine spins in the plane and allows magnetic bimeron – a topological counterpart of a skyrmion consisting two merons – to thrive.^[38,39] Recently, both Néel-type skyrmion and bimeron have been investigated in different 2D systems in the presence of magnetic anisotropy.^[19-23,31,40,41] In these reports^[42-44], an in-plane magnetic field suppresses the perpendicular magnetization and breaks the rotational symmetry, giving rise to a deformed skyrmion, a half-skyrmion, or a meron due to the expansion of spiral pitch.^[42] A perpendicular magnetic field, however, leads to a Néel-type skyrmion with rotational symmetry.^[44] Unlike switching of the magnetic easy axis, changing the direction of a magnetic field from in-plane to out-of-plane may induce transitions between different spin configurations.^[42,44] The exact type of the spin configuration depends on the material and characteristics of the magnetization. The transition leads to different topological properties as well as different transport behaviours which may benefit the design of skyrmion-based device. Therefore, a panorama of dynamic transition between different topological spin textures in 2D system is highly desirable.

In this work, we show that in a $\text{WTe}_2/\text{CrCl}_3$ bilayer vdW HS, the perpendicular MCA due to spin-orbit coupling is beneficial to the stability of the Néel-type skyrmion; so does the in-plane shape anisotropy (due to DDI) to the bimeron. Most importantly, our numerical results show that, in the presence of a perpendicular magnetic field, a skyrmion – bimeron – ferromagnetic phase transition cycle can be realized, depicted in Figure 1a. Accompanying this cyclic transition is an inversion of the topological number. Our results also show that, in comparison to the bimeron, the Néel-type

skyrmion acquires a higher velocity and a larger skyrmion Hall angle. Furthermore, we show that by depositing the HS on CuInP_2S_6 – a 2D ferroelectric substrate -- we may electrically control the writing and deletion of skyrmions via the interfacial magnetoelectric coupling.

2. Result

2.1. Lattice structure and spin model

A schematic view of the $\text{WTe}_2/\text{CrCl}_3$ bilayer is shown in Figure 1b, and details of its stacking configuration are shown in the section S1 of Supplementary Materials. The bilayer consists of a semiconducting WTe_2 monolayer and a ferromagnetic CrCl_3 monolayer stacked along the z-direction. Figure 1b depicts the top view of CrCl_3 monolayer. As a typical 2D vdW magnet, CrCl_3 monolayer has a $P-31m$ space group and consists of two Cl sublayers and one Cr sublayer on which the magnetic Cr^{3+} ions form a honeycomb lattice; the magnetic moment is $\sim 3.0 \mu_B/\text{Cr}$.^[45,46] On a free-standing CrCl_3 monolayer,^[47,48] the magnetic dipole-dipole interaction outweighs the perpendicular anisotropy induced by spin-orbit coupling, resulting in an easy-plane anisotropy and merons (with a topological number $Q = 1/2$). The DMI is absent from these free-standing films, due to the inversion symmetry. When it is in contact with an adjacent layer such as tungsten ditelluride (WTe_2), however, the inversion symmetry is broken and a finite DMI arises.^[26-29] Tungsten ditelluride (WTe_2) monolayer possesses one of the largest spin-orbit coupling among the transition metal dichalcogenides (49), which inevitably gives rise to a large DMI in $\text{WTe}_2/\text{Fe}_3\text{GeTe}_2$ (19). The nearly perfect lattice matching (lattice mismatching rate < 3%) between WTe_2 and CrCl_3 makes the bilayer heterostructure an ideal host for different types of magnetic interactions. To account for the magnetic interactions of Cr^{3+} ions, we consider the following atomically resolved Hamiltonian:

$$\begin{aligned}
 H = & - \sum_i \mu_i \mathbf{B} \cdot \mathbf{n}_i - K \sum_i (\mathbf{n}_i \cdot \hat{\mathbf{z}})^2 - J \sum_{\langle ij \rangle} \mathbf{n}_i \cdot \mathbf{n}_j - \sum_{\langle ij \rangle} \mathbf{D}_{ij} \cdot (\mathbf{n}_i \times \mathbf{n}_j) \\
 & - \frac{1}{2} \frac{\mu_0}{4\pi} \sum_{\substack{i,j \\ i \neq j}} \mu_i \mu_j \frac{3(\mathbf{n}_i \cdot \hat{\mathbf{r}}_{ij})(\mathbf{n}_j \cdot \hat{\mathbf{r}}_{ij}) - (\mathbf{n}_i \cdot \mathbf{n}_j)}{r_{ij}^3}
 \end{aligned} \quad (1)$$

where at each lattice site i the spin direction is denoted by \mathbf{n}_i , hence the magnetic moment $\mathbf{m}_i = \mu_i \mathbf{n}_i$. The first term is the Zeeman energy due to an external magnetic field \mathbf{B} . The second term denotes the single ion perpendicular anisotropy with a constant K . Ferromagnetic exchange interaction is described by the third term with a coupling constant J . DMI is described by the fourth term with a vector $\mathbf{D}_{ij} = D(\hat{\mathbf{r}}_{ij} \times \hat{\mathbf{z}})$, where D the DMI strength and $\hat{\mathbf{r}}_{ij}$ the vector connecting spins i and j . Symbol $\langle ij \rangle$ denotes that sites i and j are nearest neighbours. The last term is the magnetic dipole-dipole interaction implemented via the fast Fourier transform and convolution theorem in the *Spirit* package.^[50,51] Simulations of spin dynamics are performed by solving the Landau-Lifshitz-Gilbert (LLG) equation.^[52,53] Magnetic parameters were obtained using the first-principles density functional theory (DFT) calculation and the values of J , K and D are summarized in Table 1.^[54,55] (Details can be found in section S2 of Supplementary Materials).

2.2. Influence of magnetic field on spin textures

Micromagnetic simulations were performed on a 60×60 supercell with periodic boundary condition. The initial spin texture is obtained from a full relaxation of the paramagnetic (random) state. The spin evolution is dependent on the orientation and magnitude of the external magnetic field, which is a result of the out-of-plane polarization of the magnetic vortex core in initial state. Therefore, we focus on two field-scan schemes as shown in Figure 1c, namely, *perpendicular* (along the $+z$ or $-z$ axis) and *in-plane* (along the $+x$ axis unless otherwise specified). As we increase the magnetic field along the $+z$ direction, see Figure 1c top panel, a bimeron state appears at 60 mT and

This article is protected by copyright. All rights reserved.

it further transforms into a ferromagnetic state with a saturated magnetisation at 120 mT. Field scan along the reversed direction (i.e., along the $-z$ direction) gives rise to a Néel-type skyrmion at -120 mT; and it later transitions into the ferromagnetic state at -300 mT. As we scan the magnetic field along the $+x$ direction, the in-plane symmetry was reduced, resulting in the presence of bimeron. Magnetic field scan along the $-x$ direction also generates bimerons, but with different orientation, as Figure S2 shows. We conclude from these simulations that the perpendicular field determines the topology of the magnetic texture, namely, skyrmion or bimeron, whereas the in-plane field only tweaks the bimeron orientation.

We show in Figure 2a the spatial profile of the m_z component of an isolated Néel-type skyrmion and bimeron to highlight their topological difference. In the absence of geometric confinement, the current system requires a perpendicular MCA and additional magnetic field to provide the proper symmetry and energy gain to sustain an out-of-plane spin alignment and facilitate the formation of Néel-type skyrmions.^[35-37,56] Yet the formation of bimeron, favouring in-plane spin alignment and mainly mediated by the competition between the long-ranged dipole-dipole interaction and single ion magnetic anisotropy,^[38,39] is free from such symmetry requirement and is thus capable of surviving both perpendicular and in-plane fields. Figure 2b shows the total energy (E_{tot}) as a function of the magnetic field. The magnetic field alters the energy landscape of the system and allows the Néel-type skyrmion or bimeron formation to be energetically favourable. Our results show that the Néel-type skyrmion can only be stabilised by a perpendicular magnetic field, while bimeron can be stable in both perpendicular and in-plane magnetic fields. In addition, by comparing the bimeron energy under the magnetic fields in two directions, we found that the in-plane magnetic field brings more energy incentive. Hence, by tuning the direction or magnitude of the magnetic field, the spin texture may be modified, as a result of the coupling between the magnetic field and intrinsic magnetic properties.

Figure 2c,d show different energy components as the magnetic field varies. When the magnetic field increases along the $-z$ direction, the out-of-plane anisotropy energy (E_{MCA}) - beneficial to the stability of Néel-type skyrmion - decreases. As the magnetic field switches to the $+z$ direction, the DDI energy (E_{DDI}) decreases, which is accompanied by the presence of bimeron. This trend is particularly strong under an in-plane magnetic field, as Figure 2d shows. We therefore confirm that DDI is key to the stabilization of bimeron. (In section S4 of Supplementary Materials, we further demonstrate the role of DDI in the stabilization of bimeron by enhancing the E_{DDI}). We may draw two important conclusions from the simulation. First, by introducing a DDI, bimeron can be stabilized even in the presence of an out-of-plane anisotropy. Second, by tuning the orientation or magnitude of the magnetic field, we are able to create the desired spin textures.

2.3. Cyclic skyrmion – bimeron – ferromagnet transition

Change in spin texture in response to external stimulation discloses a magnet's functional property. Transition between skyrmion (or bimeron) and meron has recently been realized by controlling temperature or magnetic field.^[42,43,57] Yet the ideal transition should occur between skyrmion and antiskyrmion, or between skyrmion and bimeron, as meron has a non-integer topological number and is thus not topologically protected. The former (the transformation between the skyrmion and antiskyrmion) has been shown in $Mn_{1.4}Pt_{0.9}Pd_{0.1}Sn$ magnets to be controllable by in-plane magnetic field.^[44] For the latter, inspired by the magnetic field-dependent magnetic phases in our 2D system, we propose a field-controlled skyrmion – bimeron – ferromagnet transition cycle sketched in Figure 3. Under a perpendicular field of -120 mT, the system is initialised to a Néel-type skyrmion state. As the field rises from -120 mT to 60 mT (Figure 3a-d), the Néel-type skyrmion transforms to bimeron, maintaining the topological number $Q = +1$. This transformation is reversible, as our result shows. When the magnetic field rises above 120 mT, the bimeron dissolves into a

This article is protected by copyright. All rights reserved.

ferromagnetic state. Annealing process – heating and subsequent rapid cooling – is an effective means to create and stabilise the skyrmion, as numerous experiments have shown^[58-60]. Here, similar steps were simulated to excite skyrmion from ferromagnetic state: Keeping the field at 120 mT, we raise the temperature by 40 K and cool it down after a period of time, as shown in Figure 3d-g. As a result, the system is excited from the ferromagnetic state to a Néel-type skyrmion with $Q = -1$. This concludes the first half of the cycle and flips the skyrmion's topological number from $Q = +1$ (Figure 3a) to $Q = -1$ (Figure 3g). Back scanning the field from 120 mT to the initial magnitude -120 mT again converts the skyrmion (with $Q = -1$) into a bimeron (with $Q = -1$ in Figure 3j) which further disappears into a ferromagnetic state (Figure 3k); and eventually to the Néel-type skyrmion with $Q = +1$ (Figure 3a). A closed transition cycle is forged. The DMI coupling is instrumental to the transition cycle. We summarize in Figure 4 the phase diagram of the spin texture as a function of D and \mathbf{B}_z . As the magnitude of D increases, the bimeron phase moves towards a higher field; and when it varies between 0.20 and 0.28 meV, a complete transition cycle can be achieved by scanning the field from -120 mT to 120 mT.

2.4. Current-driven dynamics of skyrmion and bimeron

Skyrmion and bimeron exhibit different current-driven dynamics. Prior to the injection of current along the $+x$ direction, we placed a single Néel-type skyrmion or bimeron ($Q = +1$) onto a 200×100 supercell and let it fully relax in a magnetic field of 90 mT. A spin transfer torque of magnitude $u = jP\hbar\mu_B/(2eM_s) = 0.5 \mu\text{eV}$ was employed to simulate the in-plane current injection. This torque is proportional to the current density j and polarization P . The current-driven motion of a rigid skyrmion is described phenomenologically by a modified Thiele's equation:^[61,62]

$$\mathbf{G} \times \mathbf{v} - \alpha \mathbf{D} \cdot \mathbf{v} + 4\pi \mathbf{B} \cdot \mathbf{j} = 0 \quad (2)$$

This article is protected by copyright. All rights reserved.

where $\mathbf{G} = (0, 0, -4\pi Q)$ is the gyromagnetic coupling vector, $\mathbf{v} = (v_x, v_y)$ is the skyrmion drift velocity due to Magnus force. α is the magnetic damping parameter and \mathcal{D} is the dissipative force tensor. \mathcal{B} is the tensor related to the driving force. Equation (2) yields for the spin texture the velocity component $v_x = [-\alpha\mathcal{D} / (Q^2 + \alpha^2\mathcal{D}^2)]\mathcal{B}j$ and $v_y = [Q / (Q^2 + \alpha^2\mathcal{D}^2)]\mathcal{B}j$. For a given current density j , topological number Q and material dependent α are constants, and only the spin-configuration dependent parameters \mathcal{D} and \mathcal{B} affect the dynamics. In other words, between the Néel-type skyrmion and bimeron the difference in their transport properties mainly arises from their geometrical distinction.

Figure 5a demonstrates snapshots of the current-driven motion of Néel-type skyrmion and bimeron under the same current density. The velocities are $(v_x = 9.2 \text{ m/s}, v_y = 1.1 \text{ m/s})$ for skyrmion and $(v_x = 5.1 \text{ m/s}, v_y = 0.4 \text{ m/s})$ for bimeron. In addition, we show in Figure 5b-c the speed as a function of current density. Specifically, as the current density increases, the v_x of Néel-type skyrmion is always about twice as fast as that of bimeron, while the difference between the two becomes larger in terms of v_y , about three times. This means that, at the same speed, the Hall angle of bimeron is smaller than that of Néel-type skyrmion. Therefore, our results show that, by switching between Néel-type skyrmion and bimeron via the application of magnetic field, we can control the motion speed and direction of the topological spin texture.

2.5. Nonvolatile ferroelectric polarization controlled magnetic skyrmion

Utilising an out-of-plane electric polarization of a 2D ferroelectrics (FE), instead of a tunnelling current, to write and erase skyrmion may reduce energy dissipation in skyrmion-based devices.^[33,34] To realise such ferroelectric control, we attach a CuInP_2S_6 monolayer to the $\text{WTe}_2/\text{CrCl}_3$ HS. The ferroelectric polarization of CuInP_2S_6 can be switched by the application of an electric field, as shown in Figure 6a. The variation of CrCl_3 magnetic parameters in two different polarization states ($P+$ and

This article is protected by copyright. All rights reserved.

P^-) are summarised in Table 1. We optimized the structure from a paramagnetic state. After a full relaxation in the absence of a magnetic field, skyrmionic bubbles appear in the P^+ state, whereas the P^- is a striped state. Figure 6b shows that they may evolve, respectively, into a Néel-type skyrmion and ferromagnetic state in a perpendicular magnetic field. At a field of 120 mT, creation and annihilation of skyrmion can be achieved by switching the polarization. Such peculiarity can be explained by the polarization-induced electronic reconstruction across the interface between $WTe_2/CrCl_3$ and $CuInP_2S_6$, which is captured by the differential charge density distribution and the integral of the densities in xy -plane in Figure 6c. Compared with the P^- state (right panel of Figure 6c), the Cl ions that are in contact with the ferroelectric layer have much higher electron density in the P^+ state, leading to a higher inversion asymmetry and hence a larger DMI. Such a polarisation-induced switch in spin texture offers a rare opportunity to write and erase skyrmions electrically rather than employing a magnetic field.

3. Conclusion

In summary, we have combined first-principles calculation and micromagnetic simulation to study the magnetic configuration in a 2D $WTe_2/CrCl_3$ HS, taking into account external magnetic field, MCA, exchange interaction, DMI, and DDI. We found that MCA stabilises the Néel-type skyrmion, whereas DDI is beneficial to the formation of bimeron. By mediating the competition between two interactions, we have successfully engineered a closed skyrmion – bimeron – ferromagnet phase transition cycle. Under the same spin-polarised current, the Néel-type skyrmion and bimeron exhibit different longitudinal velocity and Hall angle. More interestingly, by interfacing the $WTe_2/CrCl_3$ HS with a $CuInP_2S_6$ monolayer, ferroelectricity-regulated writing and deletion of skyrmion can be realised via the interfacial magnetoelectric coupling. Our work opens a novel venue to the design and control of vdW-based skyrmionic devices.

This article is protected by copyright. All rights reserved.

4. Methods

4.1. The DFT method and parameters

Magnetic parameters and electronic structure were calculated by performing first-principles simulations within the DFT,^[54,55] using the projected augmented wave pseudopotentials method as implemented in the Vienna *Ab-initio* Simulation Package (VASP).^[63,64] The exchange correlation energy is calculated within the generalized gradient approximation (GGA) of Perdew-Burke-Ernzerhof form.^[65] We adopted the Dudarev approach to test the results solidity and an effective 3 eV Hubbard U_{eff} parameter is applied on Cr's d orbitals.^[66] The plane wave cutoff energy was set to 500 eV and the van der Waals interaction is included by the semiempirical DFT-D3 method.^[67] We utilized a centered $5 \times 9 \times 1$ Monkhorst-Pack k -point mesh for calculating properties of HSs, and a denser $10 \times 18 \times 1$ mesh for calculating the MCA and DMI. Utilizing the conjugate gradient method, the plane lattice constant and atomic coordinates are fully relaxed until the energy and force converge to 10^{-5} eV and 10^{-2} eV/Å, respectively. In order to eliminate the effect of periodic boundary, a 15 Å thin vacuum layer is introduced along the z direction. Spin-orbit coupling is used to calculate MCA and DMI.

4.2. Micromagnetic simulations parameters

Using *Spirit* package to simulate the spin dynamics of CrCl₃ monolayer,^[51] the time evolution of the magnetisation is described by LLG equation.^[52,53] In the presence of a spin torque,^[68,69] it reads:

$$\begin{aligned} \frac{\partial \mathbf{n}_i}{\partial t} = & -\frac{\gamma}{(1+\alpha^2)\mu_i} \mathbf{n}_i \times \mathbf{B}_i^{\text{eff}}(t) - \frac{\gamma\alpha}{(1+\alpha^2)\mu_i} \mathbf{n}_i \times [\mathbf{n}_i \times \mathbf{B}_i^{\text{eff}}(t)] + \frac{\gamma\alpha}{(1+\alpha^2)\mu_B} u \mathbf{n}_i \times \hat{\mathbf{j}} \\ & - \frac{\gamma}{(1+\alpha^2)\mu_B} u \mathbf{n}_i \\ & \times (\mathbf{n}_i \times \hat{\mathbf{j}}) \end{aligned} \quad (3)$$

where γ is the electron gyromagnetic ratio, $\alpha = 0.1$ is the damping parameter, the strength of spin transfer torque $u = jP\hbar\mu_B/(2eM_s)$ with j the current density, P is the polarization of the current, e is the electron charge, M_s is the saturation magnetization. $\hat{\mathbf{j}}$ is the electron current normal vector. The effective field with time-dependent stochastic thermal field is $\mathbf{B}_i^{\text{eff}}(t) = -\partial H/\partial \mathbf{n}_i + \mathbf{B}_i^{\text{th}}(t)$, given by

$$\mathbf{B}_i^{\text{th}}(t) = \sqrt{2D_i} \boldsymbol{\eta}_i(t) = \sqrt{2\alpha k_B T \frac{\mu_i}{\gamma}} \boldsymbol{\eta}_i(t) \quad (4)$$

where the magnitude is given by the fluctuation-dissipation theorem and $\boldsymbol{\eta}_i$ is white noise, such that the ensemble average and variance of the thermal field fulfil $\langle \mathbf{B}_{i\alpha}^{\text{th}}(t) \rangle = 0$ and $\langle \mathbf{B}_{i\alpha}^{\text{th}}(t) \mathbf{B}_{j\beta}^{\text{th}}(0) \rangle = 2D_i \delta_{ij} \delta_{\alpha\beta} \delta(t)$ respectively.

For discrete lattice, the topological charge Q is calculated using the definition of Berg and Lüscher^[70] and the following expression:

$$Q = \frac{1}{4\pi} \sum_l A_l \quad (5)$$

with

$$\cos\left(\frac{A_l}{2}\right) = \frac{1 + \mathbf{n}_i \cdot \mathbf{n}_j + \mathbf{n}_j \cdot \mathbf{n}_k + \mathbf{n}_k \cdot \mathbf{n}_i}{\sqrt{2(1 + \mathbf{n}_i \cdot \mathbf{n}_j)(1 + \mathbf{n}_j \cdot \mathbf{n}_k)(1 + \mathbf{n}_k \cdot \mathbf{n}_i)}} \quad (6)$$

where l runs over all elementary triangles of any triangulated regular lattice and A_l is the solid angle formed by the three spin vectors \mathbf{n}_i , \mathbf{n}_j and \mathbf{n}_k of the l th triangle. The sign of A_l is given by $\text{sign}(A_l) =$

This article is protected by copyright. All rights reserved.

$\text{sign}[\mathbf{n}_i \cdot (\mathbf{n}_j \times \mathbf{n}_k)]$. Note that the triangles should cover all lattice area with no overlap and \mathbf{n}_i , \mathbf{n}_j and \mathbf{n}_k should be in anticlockwise order.

Supporting Information

Supporting Information is available from the Wiley Online Library or from the author.

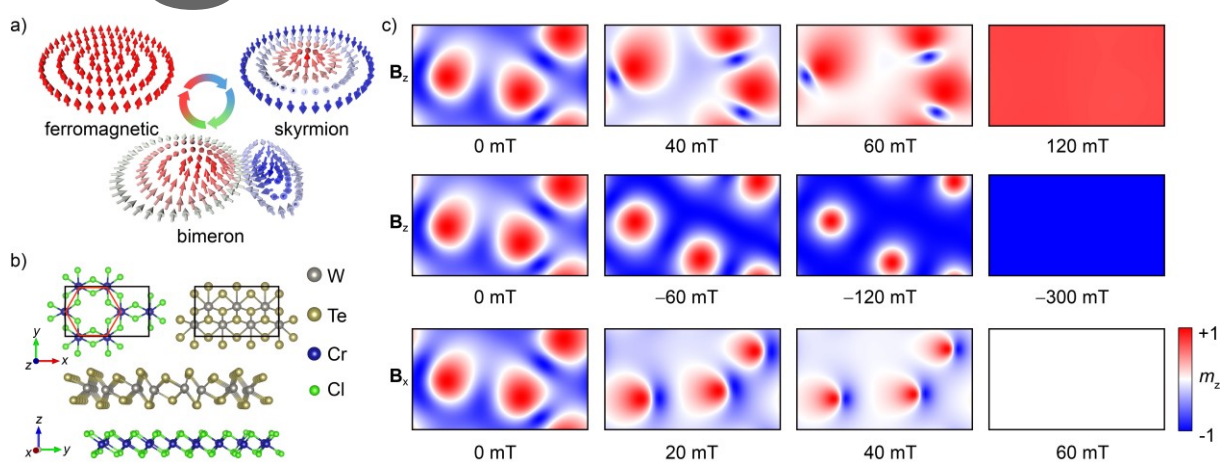
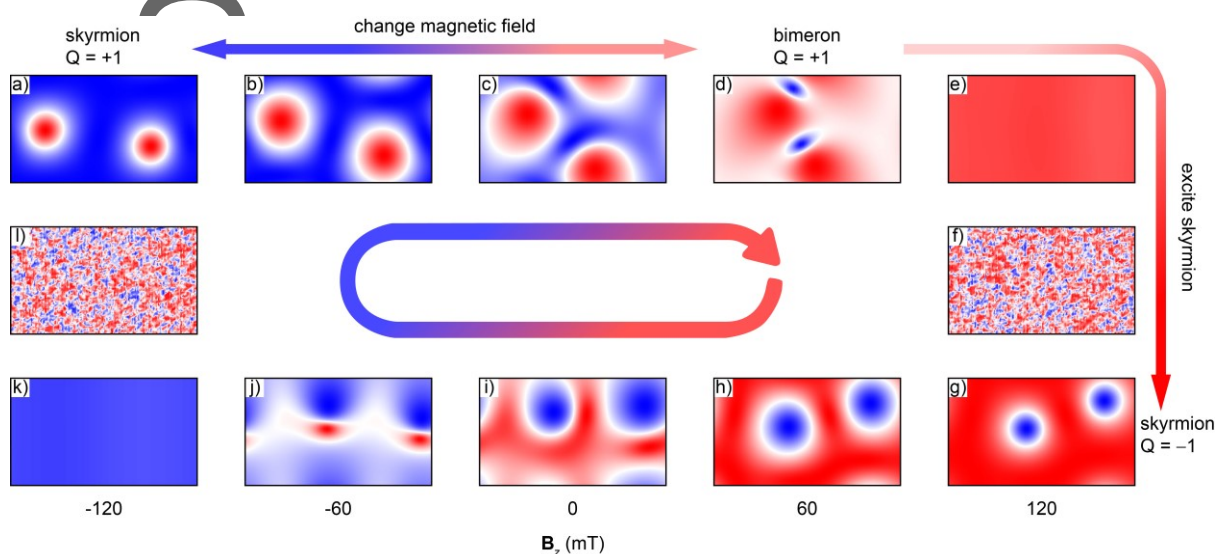


Figure 1. a) Illustration of the Néel-type skyrmion – bimeron – ferromagnet cyclic phase transition. b) Top and side views of the $\text{WTe}_2/\text{CrCl}_3$ HS. The black rectangle represents a supercell, and the red hexagon represents the honeycomb structure composed of Cr ions. c) Spin textures under perpendicular (B_z) and in-plane (B_x) magnetic fields, in 60×60 supercells.



This article is protected by copyright. All rights reserved.

Figure 3. (a-l) is a complete cycle from -120 mT to 120 mT in B_z , where a-d) and g-j) are reversible, f,l) are the spin textures when the temperature effect is considered at 40 K.

Author Manuscript

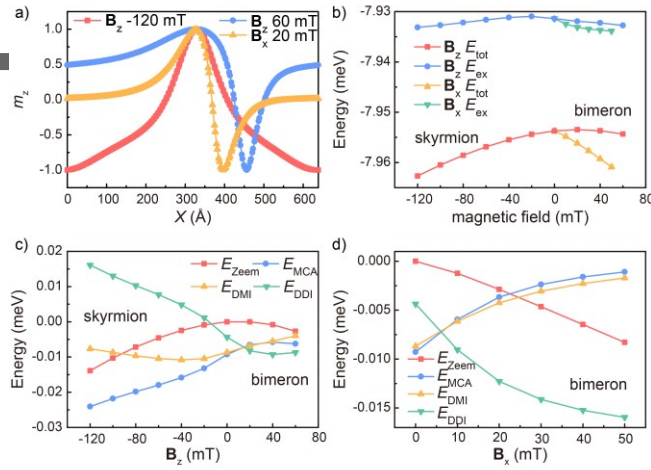


Figure 2. (a) Profile of m_z along the symmetry axis in different magnetic fields. For bimeron, we take the x axis as the symmetry axis. (b) Total energy (E_{tot}) and exchange energy (E_{ex}) as a function of magnetic field. (c), and (d) Zeeman energy (E_{zeem}), MCA energy (E_{MCA}), DMI energy (E_{MCA}), and DDI energy (E_{MCA}) as a function of B_z and B_x , respectively.

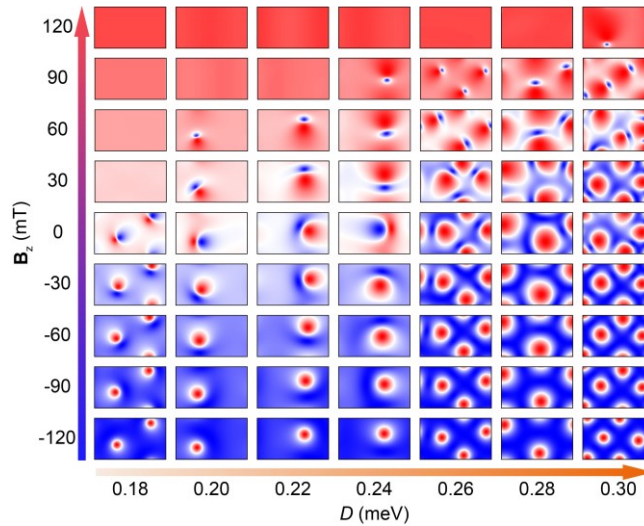


Figure 4. The spin textures with different D evolve with the magnetic field.

This article is protected by copyright. All rights reserved.

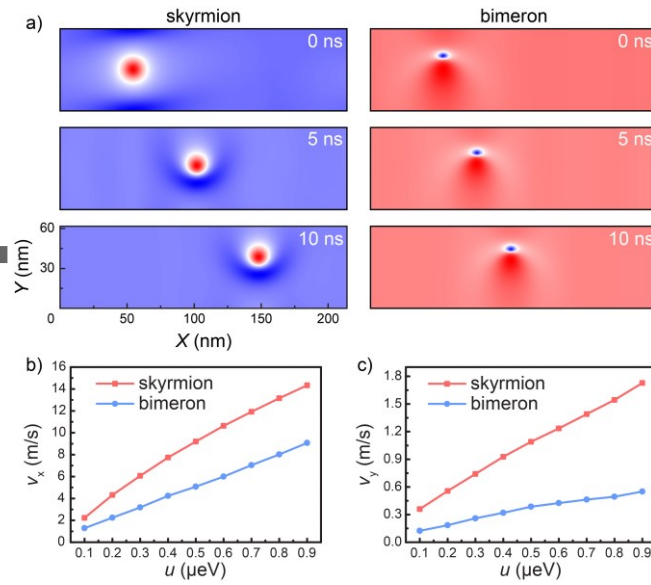


Figure 5 Dynamics of Néel-type skyrmion and bimeron driven by spin currents. (a) Snapshots of the Néel-type skyrmion and bimeron at 0 ns, 3 ns, 6 ns. (b-c) v_x and v_y as a function of spin transfer torque parameter u , respectively. This parameter u is proportional to injected current density.

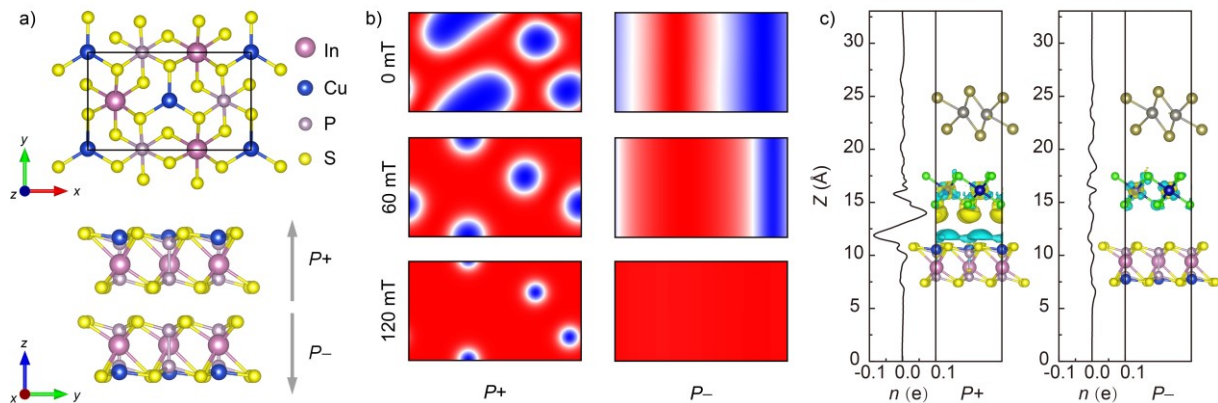


Figure 6. a) show the top and side views of the CuInP₂S₆ monolayer, the grey arrow represents the polarization direction. b) Spin textures with different polarizations. c) Differential charge density distributions of HS and the integral of the densities in xy plane (black line).

Table 1. Magnetic parameters of HSs calculated by DFT. J , K , and D represent the constant of exchange interaction, MCA and DMI, respectively. They are calculated by DFT based on the spins of unit length. r is the distance between the nearest neighbor pair of spins. $P+$ and $P-$ represent the two polarization directions in ferroelectric CuInP₂S₆ monolayer.

J (meV)	K (μeV)	D (meV)	r (Å)
-----------	-----------	-----------	---------

This article is protected by copyright. All rights reserved.

WTe ₂ /CrCl ₃	5.29	38	0.26	3.57
WTe ₂ /CrCl ₃ /P+	4.49	60	0.32	3.56
WTe ₂ /CrCl ₃ /P-	6.30	46	0.28	3.56

Acknowledgements

We acknowledge grants from the National Natural Science Foundation of China under research (Nos. 51571083 and 11674083) and Foundation of Postgraduate Education Innovation and Quality Improvement Project of Henan University (No. CX3040A0950115). Z.X. Cheng thanks Australia Research Council for support (DP190100150). H. Li acknowledges the support from the National Natural Science Foundation of China (Grant No. 11804078) and Henan University (Grant No. CJ3050A0240050). J. Z. acknowledges the financial support by the U.S. Department of Energy (DOE), Office of Science, Basic Energy Sciences (BES) under Award No. DE-SC0020221.

Competing interests

The authors declare no competing financial interest.

Received: ((will be filled in by the editorial staff))

Revised: ((will be filled in by the editorial staff))

Published online: ((will be filled in by the editorial staff))

References

- [1] U. K. Roessler, A. Bogdanov, C. Pfleiderer, *Nature* **2006**, *442*, 797.
- [2] S. Mühlbauer, B. Binz, F. Jonietz, C. Pfleiderer, A. Rosch, A. Neubauer, R. Georgii, P. Böni, *Science* **2009**, *323*, 915.
- [3] F. Jonietz, S. Mühlbauer, C. Pfleiderer, A. Neubauer, W. Münzer, A. Bauer, T. Adams, R. Georgii, P. Böni, R. A. Duine, *Science* **2010**, *330*, 1648.
- [4] N. Nagaosa, Y. Tokura, *Nature nanotechnology* **2013**, *8*, 899.
- [5] K.-S. Ryu, L. Thomas, S.-H. Yang, S. Parkin, *Nature nanotechnology* **2013**, *8*, 527.
- [6] S. Emori, U. Bauer, S.-M. Ahn, E. Martinez, G. S. Beach, *Nature materials* **2013**, *12*, 611.

This article is protected by copyright. All rights reserved.

- [7] S. Luo, M. Song, X. Li, Y. Zhang, J. Hong, X. Yang, X. Zou, N. Xu, L. You, *Nano letters* **2018**, *18*, 1180.
- [8] T. Yokouchi, S. Hoshino, N. Kanazawa, A. Kikkawa, D. Morikawa, K. Shibata, T.-h. Arima, Y. Taguchi, F. Kagawa, N. Nagaosa, *Science advances* **2018**, *4*, eaat1115.
- [9] J. Zázvorka, F. Jakobs, D. Heinze, N. Keil, S. Kromin, S. Jaiswal, K. Litzius, G. Jakob, P. Virnau, D. Pinna, *Nature nanotechnology* **2019**, *14*, 658.
- [10] N. Romming, C. Hanneken, M. Menzel, J. E. Bickel, B. Wolter, K. von Bergmann, A. Kubetzka, R. Wiesendanger, *Science* **2013**, *341*, 636.
- [11] W. Jiang, P. Upadhyaya, W. Zhang, G. Yu, M. B. Jungfleisch, F. Y. Fradin, J. E. Pearson, Y. Tserkovnyak, K. L. Wang, O. Heinonen, *Science* **2015**, *349*, 283.
- [12] K. M. Song, J.-S. Jeong, B. Pan, X. Zhang, J. Xia, S. Cha, T.-E. Park, K. Kim, S. Finizio, J. Raabe, *Nature electronics* **2020**, *3*, 148.
- [13] A. Fert, V. Cros, J. Sampaio, *Nature nanotechnology* **2013**, *8*, 152.
- [14] B. Huang, G. Clark, E. Navarro-Moratalla, D. R. Klein, R. Cheng, K. L. Seyler, D. Zhong, E. Schmidgall, M. A. McGuire, D. H. Cobden, *Nature* **2017**, *546*, 270.
- [15] C. Gong, L. Li, Z. Li, H. Ji, A. Stern, Y. Xia, T. Cao, W. Bao, C. Wang, Y. Wang, *Nature* **2017**, *546*, 265.
- [16] Y. Deng, Y. Yu, Y. Song, J. Zhang, N. Z. Wang, Z. Sun, Y. Yi, Y. Z. Wu, S. Wu, J. Zhu, *Nature* **2018**, *563*, 94.
- [17] M. Bonilla, S. Kolekar, Y. Ma, H. C. Diaz, V. Kalappattil, R. Das, T. Eggers, H. R. Gutierrez, M.-H. Phan, M. Batzill, *Nature nanotechnology* **2018**, *13*, 289.
- [18] C. Gong, X. Zhang, *Science* **2019**, *363*, 6428.
- [19] Y. Wu, S. Zhang, J. Zhang, W. Wang, Y. L. Zhu, J. Hu, G. Yin, K. Wong, C. Fang, C. Wan, *Nature communications* **2020**, *11*, 3860.
- [20] S. Laref, V. Goli, I. Smaili, U. Schwingenschlögl, A. Manchon, (preprint) *arXiv:2011.07813*, v1, submitted: nov **2020**.
- [21] Q. Cui, J. Liang, Z. Shao, P. Cui, H. Yang, *Physical review b* **2020**, *102*, 094425.
- [22] C. Xu, P. Chen, H. Tan, Y. Yang, H. Xiang, L. Bellaiche, *Physical review letters* **2020**, *125*, 037203.
- [23] M. J. Meijer, J. Lucassen, R. A. Duine, H. J. Swagten, B. Koopmans, R. Lavrijsen, M. H. Guimarães, *Nano letters* **2020**, *20*, 8563.
- [24] M.-G. Han, J. A. Garlow, Y. Liu, H. Zhang, J. Li, D. DiMarzio, M. W. Knight, C. Petrovic, D. Jariwala, Y. Zhu, *Nano letters* **2019**, *19*, 7859.
- [25] D. Amoroso, P. Barone, S. Picozzi, *Nature communications* **2020**, *11*, 5784.
- [26] X. Yu, Y. Onose, N. Kanazawa, J. Park, J. Han, Y. Matsui, N. Nagaosa, Y. Tokura, *Nature* **2010**, *465*, 901.
- [27] M. Bode, M. Heide, K. Von Bergmann, P. Ferriani, S. Heinze, G. Bihlmayer, A. Kubetzka, O. Pietzsch, S. Blügel, R. Wiesendanger, *Nature* **2007**, *447*, 190.
- [28] A. Bogdanov, U. Rößler, *Physical review letters* **2001**, *87*, 037203.
- [29] G. Chen, A. Mascaraque, H. Jia, B. Zimmermann, M. Robertson, R. L. Conte, M. Hoffmann, M. A. G. Barrio, H. Ding, R. Wiesendanger, *Science advances* **2020**, *6*, eaba4924.
- [30] Y. Zhang, C. Xu, P. Chen, Y. Nahas, S. Prokhorenko, L. Bellaiche, *Physical review b* **2020**, *102*, 241107.
- [31] C. Xu, J. Feng, S. Prokhorenko, Y. Nahas, H. Xiang, L. Bellaiche, *Physical review b* **2020**, *101*, 060404.
- [32] J. Liu, M. Shi, J. Lu, M. Anantram, *Physical review b* **2018**, *97*, 054416.

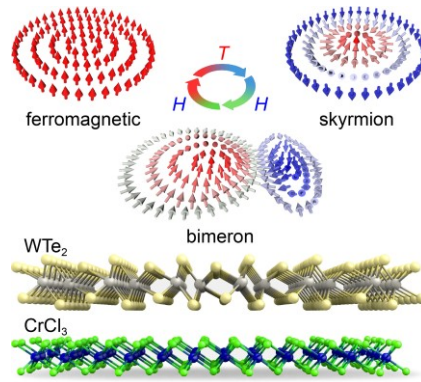
This article is protected by copyright. All rights reserved.

- [33] W. Sun, W. Wang, H. Li, G. Zhang, D. Chen, J. Wang, Z. Cheng, *Nature communications* **2020**, *11*, 5930.
- [34] C.-K. Li, X.-P. Yao, G. Chen, *Physical review research* **2021**, *3*, L012026.
- [35] J. Sampaio, V. Cros, S. Rohart, A. Thiaville, A. Fert, *Nature nanotechnology* **2013**, *8*, 839.
- [36] A. Fert, N. Reyren, V. Cros, *Nature reviews materials* **2017**, *2*, 1.
- [37] S. Woo, K. Litzius, B. Krüger, M.-Y. Im, L. Caretta, K. Richter, M. Mann, A. Krone, R. M. Reeve, M. Weigand, *Nature materials* **2016**, *15*, 501.
- [38] Y. Kharkov, O. Sushkov, M. Mostovoy, *Physical review letters* **2017**, *119*, 207201.
- [39] K.-W. Moon, J. Yoon, C. Kim, C. Hwang, *Physical review applied* **2019**, *12*, 064054.
- [40] M. Yang, Q. Li, R. Chopdekar, R. Dhall, J. Turner, J. Carlström, C. Ophus, C. Klewe, P. Shafer, A. N'Diaye, *Science advances* **2020**, *6*, eabb5157.
- [41] L. Shen, X. Li, J. Xia, L. Qiu, X. Zhang, O. A. Tretiakov, M. Ezawa, Y. Zhou, *Physical review b* **2020**, *102*, 104427.
- [42] X. Yu, W. Koshibae, Y. Tokunaga, K. Shibata, Y. Taguchi, N. Nagaosa, Y. Tokura, *Nature* **2018**, *564*, 95.
- [43] H. Jani, J.-C. Lin, J. Chen, J. Harrison, F. Maccherozzi, J. Schad, S. Prakash, C.-B. Eom, A. Ariando, T. Venkatesan, *Nature* **2021**, *590*, 74.
- [44] L. Peng, R. Takagi, W. Koshibae, K. Shibata, K. Nakajima, T.-h. Arima, N. Nagaosa, S. Seki, X. Yu, Y. Tokura, *Nature nanotechnology* **2020**, *15*, 181.
- [45] T. A. Tartaglia, J. N. Tang, J. L. Lado, F. Bahrami, M. Abramchuk, G. T. McCandless, M. C. Doyle, K. S. Burch, Y. Ran, J. Y. Chan, *Science advances* **2020**, *6*, eabb9379.
- [46] F. Xue, Y. Hou, Z. Wang, R. Wu, *Physical review b* **2019**, *100*, 224429.
- [47] M. Augustin, S. Jenkins, R. F. Evans, K. S. Novoselov, E. J. Santos, *Nature communications* **2021**, *12*, 185.
- [48] X. Lu, R. Fei, L. Zhu, L. Yang, *Nature communications* **2020**, *11*, 4724.
- [49] G.-B. Liu, W.-Y. Shan, Y. Yao, W. Yao, D. Xiao, *Physical review b* **2013**, *88*, 085433.
- [50] N. Hayashi, K. Saito, Y. Nakatani, *Japanese journal of applied physics* **1996**, *35*, 6065.
- [51] G. P. Müller, M. Hoffmann, C. Dißelkamp, D. Schürhoff, S. Mavros, M. Sallermann, N. S. Kiselev, H. Jónsson, S. Blügel, *Physical review b* **2019**, *99*, 224414.
- [52] L. Landau, E. Lifshitz, *Phy. Z. Sowjetunion* **1935**, *8*, 153.
- [53] T. L. Gilbert, *IEEE transactions on magnetics* **2004**, *40*, 3443.
- [54] P. Hohenberg, W. Kohn, *Physical review* **1964**, *136*, B864.
- [55] W. Kohn, L. J. Sham, *Physical review* **1965**, *140*, A1133.
- [56] H. Li, C. A. Akosa, P. Yan, Y. Wang, Z. Cheng, *Physical review applied* **2020**, *13*, 034046.
- [57] Y.-T. Shao, S. Das, Z. Hong, R. Xu, S. Chandrika, F. Gómez-Ortiz, P. García-Fernández, L.-Q. Chen, H. Y. Hwang, J. Junquera, (preprint) *arXiv:2101.04545*, v2, submitted: Jan **2021**.
- [58] C. Jin, Z.-A. Li, A. Kovács, J. Caron, F. Zheng, F. N. Rybakov, N. S. Kiselev, H. Du, S. Blügel, M. Tian, *Nature communications* **2017**, *8*, 15569.
- [59] H. Oike, A. Kikkawa, N. Kanazawa, Y. Taguchi, M. Kawasaki, Y. Tokura, F. Kagawa, *Nature physics* **2016**, *12*, 62.
- [60] A. Chacon, L. Heinen, M. Halder, A. Bauer, W. Simeth, S. Mühlbauer, H. Berger, M. Garst, A. Rosch, C. Pfleiderer, *Nature physics* **2018**, *14*, 936.
- [61] W. Jiang, X. Zhang, G. Yu, W. Zhang, X. Wang, M. B. Jungfleisch, J. E. Pearson, X. Cheng, O. Heinonen, K. L. Wang, *Nature physics* **2017**, *13*, 162.
- [62] A. Thiele, *Physical review letters* **1973**, *30*, 230.
- [63] G. Kresse, J. Hafner, *Physical review b* **1993**, *47*, 558.

This article is protected by copyright. All rights reserved.

- [64]G. Kresse, J. Furthmüller, *Physical review b* **1996**, *54*, 11169.
- [65]J. P. Perdew, K. Burke, M. Ernzerhof, *Physical review letters* **1996**, *77*, 3865.
- [66]S. Dudarev, G. Botton, S. Savrasov, C. Humphreys, A. Sutton, *Physical review b* **1998**, *57*, 1505.
- [67]S. Grimme, J. Antony, S. Ehrlich, H. Krieg, *The journal of chemical physics* **2010**, *132*, 154104.
- [68]W. F. Brown Jr, *Physical review* **1963**, *130*, 1677.
- [69]C. Schieback, M. Kläui, U. Nowak, U. Rüdiger, P. Nielaba, *The European physical journal b* **2007**, *59*, 429.
- [70]B. Berg, M. Lüscher, *Nuclear physics b* **1981**, *190*, 412.

Author Manuscript



In the $WTe_2/CrCl_3$ bilayer vdW heterostructure, a perfect Néel-type skyrmion – bimeron – ferromagnetic cyclic phase transition featured by the evolution of the topological number was achieved by resorting to a perpendicular magnetic field combined with heating and cooling, and the skyrmion can be written and erased by the ferroelectricity of $CuInP_2S_6$ monolayer.